ADVANCED ELECTRONIC MATERIALS
Open Access
www.advelectronicmat.de

Investigating the Electromechanical Behavior of Unconventionally Ferroelectric $Hf_{0.5}Zr_{0.5}O_2$-Based Capacitors Through Operando Nanobeam X-Ray Diffraction

Evgenios Stylianidis, Pranav Surabhi, Ruben Hamming-Green, Mart Salverda, Yingfen Wei, Arjan Burema, Sylvia Matzen, Tamalika Banerjee, Alexander Björling, Binayak Mukherjee, Sangita Dutta, Hugo Aramberri, Jorge Íñiguez, Beatriz Noheda, Dina Carbone, and Pavan Nukala**

Understanding various aspects of ferroelectricity in hafnia-based nanomaterials is of vital importance for the development of future nonvolatile memory and logic devices. Here, the unconventional and weak electromechanical response of epitaxial $La_{0.67}Sr_{0.33}MnO_3/Hf_{0.5}Zr_{0.5}O_2/La_{0.67}Sr_{0.33}MnO_3$ ferroelectric capacitors is investigated, via the sensitivity offered by nanobeam X-ray diffraction experiments during application of electrical bias. It is shown that the pristine rhombohedral phase exhibits a linear piezoelectric effect with piezoelectric coefficient ($|d_{33}|$) ≈ 0.5–0.8 pmV^{-1}. It is found that the piezoelectric response is suppressed above the coercive voltage. For higher voltages, and with the onset of DC conductivity throughout the capacitor, a second-order effect is observed. The work sheds light into the electromechanical response of rhombohedral $Hf_{0.5}Zr_{0.5}O_2$ and suggests its (un)correlation with ferroelectric switching.

1. Introduction

For more than a decade now, hafnia-based nanomaterials are justifiably among the most studied materials in the field of ferroelectrics and microelectronics, both from a fundamental and an application perspective.[1,2] Hafnia and its compounds show a unique type of ferroelectricity that becomes robust at the nanoscale,[3] unlike traditional perovskite ferroelectrics that suffer from depolarization effects at reduced dimensions.[4] The discovery of ferroelectricity in hafnia, combined with its silicon compatibility, initiated a new wave of studies for novel ferroelectric memories and logic nanodevices.[5,6]

E. Stylianidis
Department of Physics and Astronomy
University College London
Gower Street, London WC1E 6BT, United Kingdom

P. Surabhi, P. Nukala
Center for Nanoscience and Engineering
Indian Institute of Science
Bengaluru 560012, India
E-mail: pnukala@iisc.ac.in

R. Hamming-Green, M. Salverda, A. Burema, T. Banerjee, B. Noheda
Zernike Institute for Advanced Materials
University of Groningen
Groningen 9747 AG, The Netherlands

Y. Wei
Frontier Institute of Chip and System
Fudan University
No. 2005 Songhu Road, Yangpu District, Shanghai 200438, China

The ORCID identification number(s) for the author(s) of this article can be found under https://doi.org/10.1002/aelm.202201298.

DOI: 10.1002/aelm.202201298

S. Matzen
Center for Nanoscience and Nanotechnology
Department of Materials
Paris-Saclay University
CNRS
Palaiseau 91120, France

A. Björling, D. Carbone
MAX IV Laboratory
Lund University
PO Box: 118, Lund SE- 221 00, Sweden
E-mail: gerardina.carbone@maxiv.lu.se

B. Mukherjee, S. Dutta, H. Aramberri, J. Íñiguez
Department of Materials Research and Technology
Luxembourg Institute of Science and Technology (LIST)
Esch/Alzette L-4362, Luxembourg

J. Íñiguez
Department of Physics and Materials Science
University of Luxembourg
Belvaux L-4422, Luxembourg

B. Noheda
CogniGron Center
University of Groningen
Groningen 9747 AG, The Netherlands

Understanding the stabilization of a ground-state ferroelectricity at the nanoscale, as well as the physical mechanism behind ferroelectric switching in this peculiar ferroelectric, has proved far from trivial. The most usually reported phase of ferroelectric hafnia is a metastable polar orthorhombic (*o*-) phase,[2] while a polar rhombohedral (*r*-) phase has been stabilized under certain conditions when $La_{0.67}Sr_{0.33}MnO_3$ (LSMO)-buffered $Hf_{0.5}Zr_{0.5}O_2$ (HZO) is grown on $SrTiO_3$ (STO) substrates.[7] Interestingly, as demonstrated by integrated differential phase contrast scanning transmission electron microscopy (iDPC STEM),[8] this *r*-phase lacks the polar/nonpolar sublayer structure that has been reported to be responsible for the flat-phonon band and, thus, for the dipolar localization that possibly gives rise to unconventional, noncooperative, switching behavior of ferroelectric hafnia.[9] Furthermore, the remnant polarization in this phase arising from the polar nature of the *R3m* phase, which itself is stabilized by oxygen deficiency, is <9 μCcm^{-2}.[9] Nevertheless, macroscopic ferroelectric characterization on 5-nm thick *r*-phase samples showed very large switching currents corresponding to having a remnant polarization of ≈35 μCcm^{-2}, comparable to or larger than those observed in *o*-phase hafnia.[10] This discrepancy has been resolved through in-situ electron microscopy experiments that clearly showed that polarization switching is intertwined with oxygen vacancy migration, and is different from normal ferroelectrics.[8,11] In other words, ferroelectric switching in hafnia is driven by polarization switching with electrochemical origins. We will refer to this as electrochemical polarization. Whether the crystal polarization is decoupled to electrochemical polarization or uncorrelated to it is still an open question.

Conventional ferroelectric switching (crystal polarization switching) is accompanied by an electromechanical response, characterized by butterfly-like strain versus electric field loops. Understanding the electromechanical response of unconventional hafnia-based ferroelectrics can give more insights into the origins of ferroelectricity. However, despite the massive interest in the ferroelectric properties of hafnia-based materials, the explorations on electromechanical behavior are still in the nascent stages. Electrostrain measurements on thick polycrystalline La:HfO_2 films reported by Schenk et al. show a classic ferroelectric butterfly loop, with the upturns in the strain curve occurring at the coercive field, and a positive piezoelectric coefficient $d_{33} \approx 7.7$ pmV^{-1}.[12] Recent theoretical and experimental works reported that a negative longitudinal piezoelectric coefficient is possible in the orthorhombic phase of HfO_2, a behavior that is usually found in organic ferroelectrics.[13–15] More interestingly, first-principles simulations predict that the sign of the piezoelectric coefficient d_{33} can be reversed by tuning the local environment without affecting the global polar *o*-phase symmetry or switching its polarization.[15]

Point defects and defect-migration-induced giant electrostriction have recently gained tremendous attention in sister compounds of hafnia such as doped ceria and bismuth oxide.[16,17] "Giant" electrostriction has been first reported in 20% Gd-doped CeO_2 in 2012. The response of electroactive defect complexes in nondilute concentrations to an external electric field, and their corresponding elastic dipoles result in substantial long-range electrostrain.[18,19] Such an effect is second order in nature or electrostrictive. Glinchuk et al.[20] suggest through a Landau–Ginzburg–Devonshire framework that such an electrostrictive effect can even create a switchable chemical polarization in hafnia-based materials. The switching characteristics of *r*-phase hafnia have similar defect-migration-based origins.[8] Thus, it is paramount to understand the electromechanical behavior of these systems, and enquire further into the origin of the observed switching currents in hafnia-based systems, and their possible coupling or decoupling with the crystal polarization.

In this report, we present results from synchrotron diffraction experiments during application of external bias on $La_{0.67}Sr_{0.33}MnO_3/Hf_{0.5}Zr_{0.5}O_2/La_{0.67}Sr_{0.33}MnO_3$ capacitors grown epitaxially on (001)-oriented $SrTiO_3$ substrates. By following the evolution of the diffraction peaks of our materials hand-in-hand with a bursting voltage scheme, we probe the electrostrain behavior of the thin films at various applied fields. We show that *r*-phase HZO exhibits only a linear piezoresponse at voltages even larger than the coercive voltage. A second-order response appears at much higher voltages where leakage or DC conductivity is significant. Our work shows that electrochemical polarization is uncorrelated with crystal polarization. We ascribe the second-order response to effects such as Joule heating and defect migration.

2. Results and Discussion

2.1. Electrical Precharacterization and Crystalline Coherence

LSMO/HZO/LSMO capacitors compatible with operando-biasing experiments were fabricated using photolithography-based techniques (see Experimental Section). **Figure 1**a depicts the positive up/negative down (PUND)-corrected current response as a function of the applied voltage, showing the characteristic polarization-switching peaks, as previously identified for this system.[7]

Figure 1b shows representative X-ray diffraction (XRD) specular diffractograms before (virgin) and after (cycled) the synchrotron experiment, including several cycles of voltage biasing. The XRD spectra show clearly a well-defined (001) Bragg peak from the bottom LSMO layer at $2\theta = 20.76^o$, the (111) peak from the HZO layer at $2\theta = 26.60^o$, and the (110) peak from the top LSMO layer at $2\theta = 28.96^o$. The presence of well-defined intensity oscillations (Laue oscillations) reveals the highly crystalline coherence of the system. Oscillations with two different periods can be observed: the short period around the (001) LSMO Bragg peak is relative to a thickness of around 35 nm, while the larger period originates from the 5-nm thick HZO (111) layer. The top layer of LSMO (also 35-nm thick) is highly oriented along the pseudocubic (p.c.) direction $<110>_{p.c.}$. A good simulation of the diffractograms was obtained using a model proposed by Lichtensteiger,[21] based on the kinematic theory. The as-deposited samples show a crystallographic polarization pointing toward the top LSMO layer (or "polarization up," see ref. [8]). We note, however, that the subsequent experiments were performed after "prepoling" the device with a voltage pulse of +3 V.

ADVANCED ELECTRONIC MATERIALS
Open Access
www.advelectronicmat.de

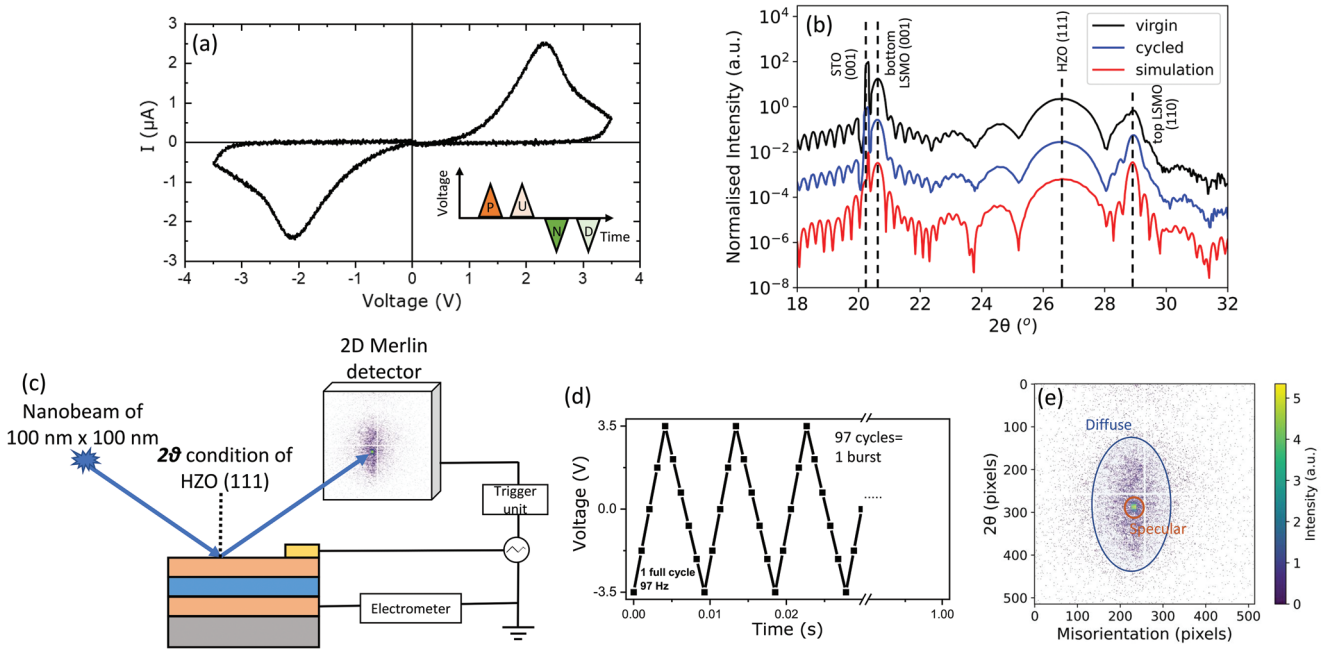

Figure 1. a) PUND-corrected macroscopic electrical characterization performed offline, using a 1 kHz triangular voltage pulses scheme (inset). b) Specular X-ray diffractograms of the device under test at the virgin and cycled states, as well as a simulated curve. The curves are offset for clarity. c) Schematic illustration of the experimental setup used during the operando synchrotron experiment. d) Triangular voltage pulses with 97 Hz are used. Black squares represent the times where X-ray frames are acquired. e) Snapshot of typical data on the two-dimensional detector: the diffuse and the high-intensity specular part of the HZO (111) Bragg peak are highlighted.

2.2. Operando Diffraction Experiment

A diffraction experiment while applying an electrical bias was performed at the diffraction endstation of the NanoMAX beamline of MAX IV Laboratory in Lund, using a 100-nm diameter beam and a wavelength of 1.379 Å. The setup of the experiment is graphically illustrated in Figure 1c. Triangular voltage waveforms varying from $-V_{max}$ to V_{max} of 97 Hz were applied in 50–60 successive bursts, always grounding the bottom electrode. Structural data were acquired every millisecond on a 2D detector aligned at $2\theta = 26.60°$, which is the (111) Bragg peak of HZO. In this setup, any HZO (111) lattice parameter variation translates into a subtle movement of the Bragg peak along the vertical axis on the 2D detector. The instantaneous displacement current was simultaneously measured using an electrometer capable of detecting nA currents.

The signal on the detector image contains two contributions (Figure 1e): a sharp central peak, which arises from the crystal truncation rod of the coherent heterostructure, and a broad diffuse intensity (along the 2θ axis) that is generated by the HZO film and relates to the lattice spacing of the HZO (111) planes (d_{111}). We followed in situ the evolution of the diffuse intensity during the application of the triangular voltage wave, by acquiring data with a frequency about ten times higher than the voltage pulses. The 97 Hz frequency was chosen to reduce the occurrence of artifacts due to the sole acquisition scheme. The measurement of repeated bursts was used to improve the signal-to-noise ratio by integrating all the images corresponding to the same voltage (this is practically done by associating to each dataset a specific time-stamp over all the bursts). The collection of such large statistics, combined with the intrinsically high-strain resolution provided by the X-ray diffraction, allowed us to determine the variation of the lattice parameter by tracking the changes of center of mass (COM) of the (111) peak with the applied bias, to a precision of <0.01 pm. The use of a focused beam was necessary to locate the μm size device on the large-sample support and to check heterogeneity of behavior in the device. Owing to the sample being aligned at the (111) Bragg peak, the effective size of the beam on the inclined sample was 400 nm along the direction of propagation (vertical, in the geometry used).

Representative results from the operando experiments are presented in **Figure 2**a,b for two selected voltage amplitudes. For the case of a voltage amplitude of 2 V, we observe a small linear change of the lattice constant. Fourier transform (FT) analysis of the lattice parameter variation over time, Figure 2a,b, for a repeated number of bursts, shows a single peak at 97 Hz, corresponding to the drive voltage frequency, confirming that the XRD effectively captures a lattice variation caused by the applied voltage. We note that the linear behavior is observed for all voltage amplitudes below and up to 2 V (Figure S2, Supporting Information); however, at 2.8 V, the peak at 97 Hz in the FT disappears, indicating almost no change in the HZO (111) lattice parameter with voltage. These results are uniform across the device area, reproducible, and do not depend on the sample history.

To quantify the changes in the lattice parameter of HZO, we performed a linear fit of the lattice constant versus voltage curves and estimated $|d_{33}|$ at various maximum voltages as shown in Figure 2c. Within the fitting error, we

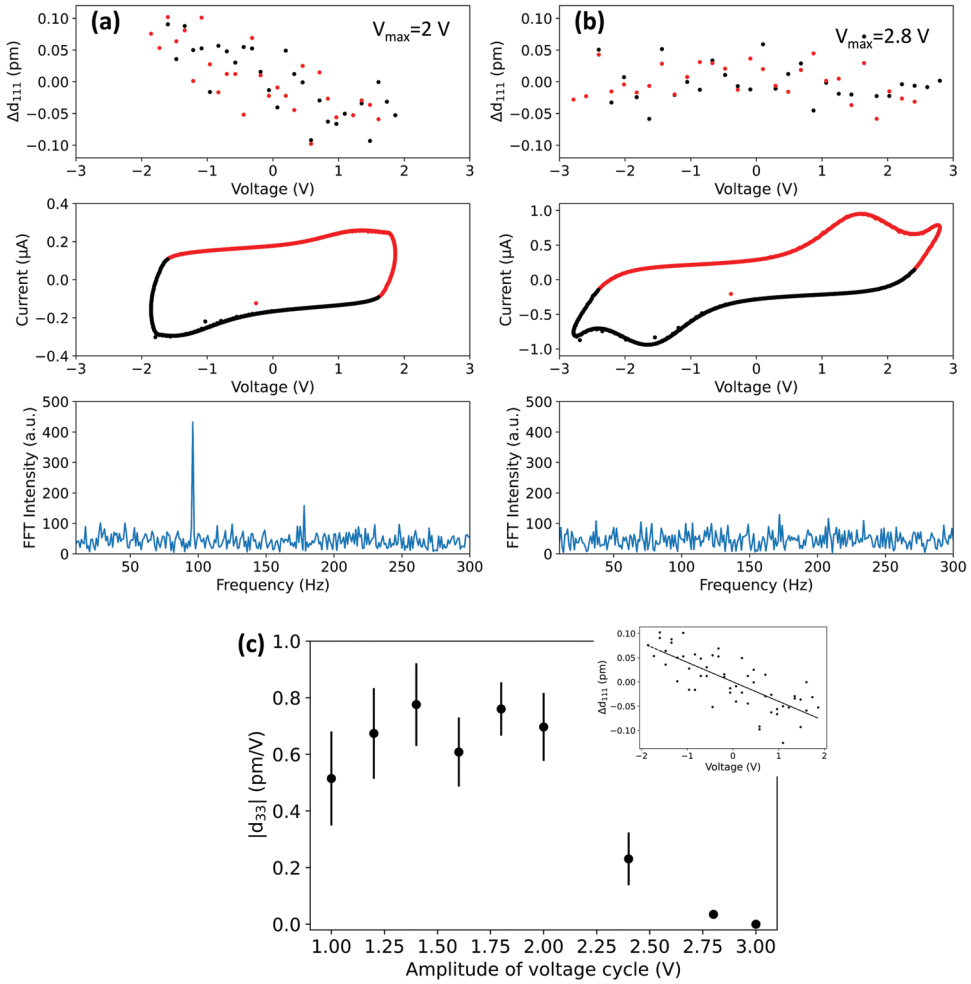

Figure 2. Measurements of the unit-cell strain performed by applying an amplitude of: a) 2 V and b) 2.8 V. Top: variation of lattice parameters of HZO as extracted from the shift in reciprocal space of the HZO (111) reflection. Middle: the *I–V* curves as measured by the electrometer during the diffraction experiment. Red and black points/lines represent the data collected from positive and negative going voltage cycles, respectively. Bottom: Fourier transform of the temporal evolution of the HZO (111) COM over the whole measurement. c) The longitudinal piezoelectric coefficients $|d_{33}|$ as calculated from linear fits of the lattice parameter response to each of the applied voltages (inset) as a function of the amplitude of the applied voltage.

observe that $|d_{33}|$ does not change significantly up to 2 V and ranges between 0.5 and 0.8 pmV^{-1}. At 2.4 V, $|d_{33}|$ decreases to 0.3 pmV^{-1} and becomes zero at 2.8 V. It is important to note that the observed reduction in $|d_{33}|$ for V_{max} >2 V occurs when the current switching peak starts becoming apparent in the displacement current, as observed in the *I–V* characteristics that were simultaneously measured during the burst experiment (Figure 2a,b). Note that, when V_{max} is above the coercive voltage, in the range 2–2.8 V, the device does not show conventional ferroelectric butterfly-type strain response, rather still shows a simple linear weak piezoelectric response. Imprint effects could cause an asymmetric response in conventional ferroelectrics,[22] but we do not see any evidence of imprint in our P-E loops. These observations suggest that the ferroelectric switching in our samples is unconventional in nature.

For even higher voltages (>2.8 V), the electromechanical response of HZO shows both a first- and a significant second-order behavior (**Figure 3**), as clearly revealed by the appearance of two peaks, at 97 Hz and at 194 Hz in the Fourier transform. Repeated burst measurements at the same voltage show the repeatability of this response. It is important to note that the onset of this second-order behavior is uncorrelated from the ferroelectric switching. This correlates, however, with the leakage behavior at large fields (V_{max} = 3.2 V and above) and increases with increasing leakage. We confirmed this by measuring the electromechanical response of damaged highly leaky capacitors that still show the 194 Hz peak in the Fourier transform (Figure 3).

2.3. Discussion-Model and Physical Behavior

Our results suggest two distinct regimes of electromechanical response in our devices. At low fields, we observe a negative linear response, consistent with a weak piezoelectric response of a weakly polar *r*-phase. However, as the amplitude of the applied bias increases, the electromechanical response decreases and it is strongly reduced when the applied bias is large enough to complete the polarization-switching process. Surprisingly, for applied voltages higher than the coercive voltage, only a small

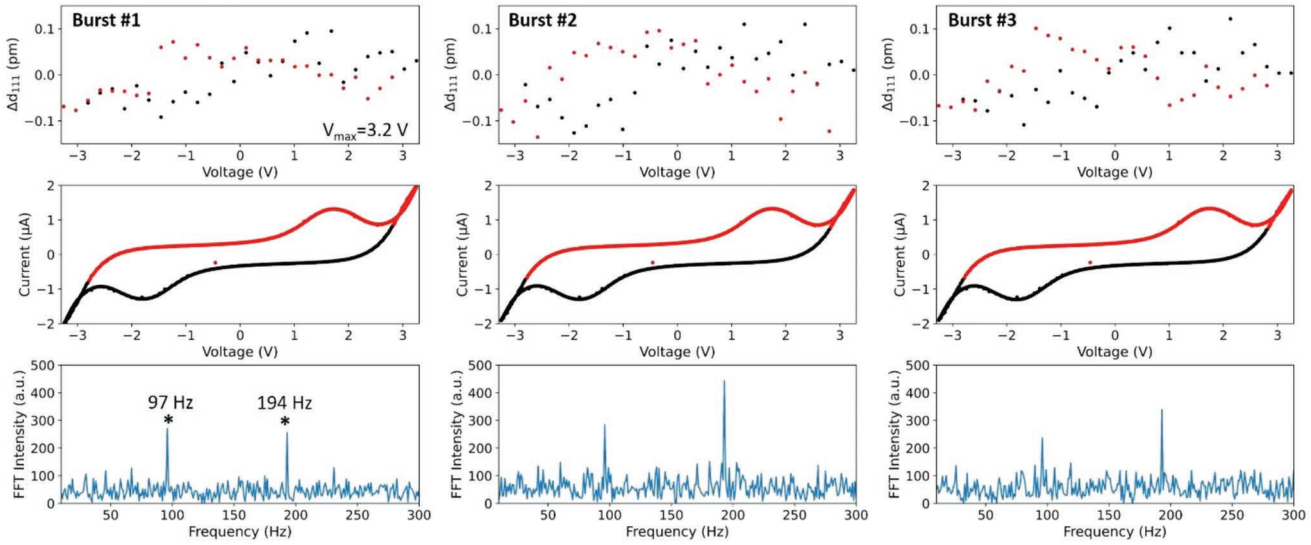

Figure 3. Repeated unit-cell strain measurements with voltage amplitude of 3.2 V. Top: the variation of HZO (111) out-of-plane lattice parameter. Middle: the instantaneous *I*–*V* response during the experiment. Bottom: the calculated Fourier transform of the lattice parameter variation.

linear behavior is observed (i.e., Figure S2, Supporting Information, for an applied bias of 2.4 V). This clearly shows that the electromechanical response is unlike that of conventional ferroelectrics, which show the onset of second-order behavior corresponding to the crystal polarization-switching kinetics of domain nucleation and growth. The second-order response observed in our samples occurs at much larger voltages (V_{max} > 2.8 V), where leakage becomes significant. Leakage-induced second-order strain effects include Joule heating and nonclassical electrostriction (through ion migration) and these mechanisms can explain the high-field behavior of our devices.[16,23]

We use first-principles techniques to compute the intrinsic piezoresponse of the *r*-phase HZO (see Experimental Section). We obtain a value of d_{33} = –7.6 pmV^{-1} for a strain-state that has a positive polarization of 1.01 μCcm^{-2} along the rhombohedral axis. The selected strain state corresponds to the defect-free *R3m* phase, with the lattice parameters measured experimentally. Our earlier electron microscopy studies indicate, however, that our samples indeed are stabilized in a low-strain *R3m* phase albeit with oxygen vacancies.[7] Without considering the presence of oxygen vacancies, the *R3m* phase has a very low crystal polarization, as calculated from DFT.[7] Inclusion of oxygen vacancies allowed us to estimate the crystal polarization values ≈9 μCcm^{-2}.[8] The full elastic and piezoelectric tensors computed from first-principles here are thus on defect-free *R3m* phase, and are provided in Tables S1–S3 (Supporting Information).

We would like to note that quantifying the piezoelectric behavior of the *R3m* phase in the selected strain of d_{111} ≈ 3 Å using our methods is far from trivial. The negative piezoelectric coefficient calculated from our perturbative (accurate) methods here may look contradictive to our previous "finite-difference" (rough) estimates of a positive d_{33} of ref. [7]. We found that this inconsistent behavior arises due to the competition of nonstandard and nontrivial coupling modes controlling the improper ferroelectricity of this phase. Elaborating a physically meaningful mechanism of piezoelectricity of the *R3m* phase in small strains, as it was the case for the o-phase for example in ref. [15], falls out of the scope of the current study and we refer to a future work (Dutta et al., in progress). At any rate, our calculations do yield an intrinsic anomalous longitudinal piezoresponse. The amplitude of the computed effect is about seven times larger than the measured one, and it should be considered an upper limit corresponding to an ideal (infinite, periodic) film where size effects are not considered.

Additionally, let us note that it is unclear how to compute the extrinsic contribution to the piezoresponse from atomistic simulations; this would crucially depend on the particular extrinsic mechanism (such as the migration of oxygen vacancies) considered, and falls beyond the scope of this work. As a result, we remain agnostic about the exact sign of d_{33} in our experimental defective *R3m* samples.

Our previous experiments[8] revealed that polarization switching is intertwined with oxygen vacancies migration, and has electrochemical origins. This work further shows evidence that the electromechanical response is decoupled from ferroelectric switching, supporting unconventional origins of ferroelectricity in these samples. Furthermore, any effect related to ionic migration cannot be neglected from the electromechanical response in the high voltage regime, above the coercive field. For instance, defects and ionic migration can give rise to nonclassical piezoelectricity and electrostriction, as found in sister fluorite compounds of hafnia such as Gd-doped CeO_2[16,19,23] and (Y, Nb)-stabilized Bi_2O_3.[17]

3. Conclusions

We investigated the electromechanical behavior of *r*-phase HZO via operando synchrotron studies using high-flux nanofocused X-ray beam diffraction. At low fields, our results revealed a linear piezoresponse with $|d_{33}|$ ≈ 0.5–0.8 pmV^{-1}, which is related to intrinsic piezoelectricity in rhombohedral HZO. Even above the coercive voltage, we still observe only first-order

response, albeit weakened further, and the absence of a conventional ferroelectric butterfly loop. We also show that leakage directly correlates with the second-order strain response (at even high voltages) with possible origins in Joule heating or ion migration. Our findings clearly lend credence to the previous works that show that ferroelectricity in *r*-phase HZO is unconventional and driven by oxygen vacancy migration and electrochemistry.

4. Experimental Section

Growth: The materials $La_{0.7}Sr_{0.3}MnO_3$ (30 nm)/$Hf_{0.5}Zr_{0.5}O_2$ (6 nm)/$La_{0.7}Sr_{0.3}MnO_3$ (30 nm) were grown on (001)-oriented $SrTiO_3$ substrates by pulsed laser deposition (PLD) as described elsewhere.[7]

Device Fabrication: The fabrication flow diagram of the devices can be found elsewhere.[8] Square capacitors with an area of 50 µm x 50 µm were patterned using standard photolithography and Ar-ion milling. The capacitors were electrically connected to Ti/Au contacting pads, while their surface was kept optically clear to be probed with the nanobeam. The contacting pads were then Au wire bonded to chip carriers.

Macroscopic Electrical Characterization: The capacitors were electrically tested in the lab prior the synchrotron experiment using the standard PUND (positive-up-negative-down) measurement scheme (inset of Figure 1a). Triangular pulses of 1 kHz in frequency and 3.5 V in amplitude were used, with a delay time of 250 µs in between each pulse. The data presented in Figure 1a is the PUND-corrected data: the current response during the up (down) pulse was subtracted from the current response of the positive (negative) pulse, resulting in a current response that contained only the displacement current. A Keithley 4200A-SCS parameter analyzer equipped with Source Measure Units (SMUs) and a Pulse Measurement Unit (PMU) was used for the measurement.

In-Situ Biasing Burst Diffraction Experiment: The operando experiments were performed at the NanoMAX beamline of the MAX IV Laboratory in Lund, Sweden.[24] Following a synchronisation scheme developed elsewhere[25] beam of wavelength 1.379 Å and a beam size of 100 nm in diameter was used. A burst voltage scheme was used consisting of triangular pulses of 97 Hz frequency while acquiring X-ray images and current measurements at 1 kHz. A R&S HMF2550 pulse generator was used for the formation of the biasing train, and an electrometer (ALBA) was used to measure the current, while the bias was sampled with a PandABox (Quantum Detectors) acquisition unit. A two-dimensional Merlin detector (Quantum Detectors) was used, which was at a fixed position during the bursting experiment, corresponding to the 2θ angle of the main Bragg peaks of the films.

First-Principles Calculations: Density functional theory (DFT) calculations were performed as implemented in the Vienna Ab initio Simulation Package (VASP).[26,27] For the exchange-correlation functional, the Perdew–Burke–Ernzerhof formulation for solids (PBEsol)[28] of the generalized gradient approximation (GGA) was used. The atomic cores were treated within the projector-augmented wave approach,[28] considering the following states explicitly: 5p, 6s, and 5d for Hf; 4s, 4p, 4d, and 5s for Zr; and 2s and 2p for O. An 800 eV energy cutoff was used for the plane-wave basis set. Brillouin zone integrals were computed in a $4 \times 4 \times 1$ Gamma-centered k-point grid corresponding to a simulation supercell of 72 atoms. The hafnium and zirconium atoms were arranged in alternating layers along the [111] rhombohedral direction in order to preserve the *R3m* symmetry of the *r*-phase. The d_{111} lattice spacing was fixed to the experimentally observed value of 2.99 Å, and the structure was allowed to relax under this constraint until residual forces fell below 0.01 eVÅ^{-1}. The piezoresponse tensor was computed using density functional perturbation theory (DFPT)[30] as readily implemented in VASP. The elastic tensor (which the authors used to obtain the piezoelectric strain tensor *d* from the DFPT-computed piezoelectric stress tensor *e*) was obtained using a finite-differences scheme, with each degree of freedom perturbed by 0.015 Å. The polarization was computed using the Berry phase approach within the modern theory of polarization.[31]

Supporting Information

Supporting Information is available from the Wiley Online Library or from the author.

Acknowledgements

The authors acknowledge MAX IV Laboratory for time on Beamline NanoMAX under Proposal 20190954. Research conducted at MAX IV, a Swedish national user facility, was supported by the Swedish Research Council (under contract grant No. 2018—07152), the Swedish Governmental Agency for Innovation Systems (under contract grant No. 2018–04969), and Formas (under contract grant No. 2019–02496). Work at LIST was supported by the Luxembourg National Research Fund though (grant Nos. INTER/NOW/20/15079143/TRICOLOR (to B.M., H.A., J.I.) and PRIDE/15/10935404/MASSENA (to S.D.). P.N. acknowledges national nanofabrication and micro-nano characterization facilities at the center for nanoscience and engineering, IISc. P.N. also acknowledges SERB grant (SRG/000285) and Infosys Young Scientist Award. B.N. and T.B. acknowledge the financial support of the CogniGron research center and the Ubbo Emmius Funds (University of Groningen). Device fabrication were realized using NanoLab NL facilities. S.M. acknowledges the support from the French RENATECH network for the research at the Center for Nanoscience and Nanotechnology.

Conflict of Interest

The authors declare no conflict of interest.

Data Availability Statement

The data that support the findings of this study are available from the corresponding author upon reasonable request.

Keywords

electrochemical polarization, first-principles, nanobeam diffraction, rhombohedral $Hf_{0.5}Zr_{0.5}O_2$

Received: December 7, 2022
Revised: March 8, 2023
Published online:

[1] T. S. Böscke, J. Müller, D. Bräuhaus, U. Schröder, U. Böttger, *Appl. Phys. Lett.* **2011**, *99*, 102903.
[2] U. Schroeder, C. Seong Hwang, H. Funakubo, Eds., *Ferroelectricity in Doped Hafnium Oxide: Materials, Properties and Devices*, Woodhead Publishing, Duxford, UK **2019**.
[3] S. Hsu, J. Xiao, H. Zhang, R. Wagner, A. Datar, M. R. Mccarter, C. R. Serrao, A. K. Yadav, G. Karbasian, C. Hsu, A. J. Tan, L. Wang, V. Thakare, X. Zhang, A. Mehta, *Nature* **2020**, *580*, 478.
[4] C. Lichtensteiger, M. Dawber, J. Triscone, in *Physics of Ferroelectrics*, Springer-Verlag, Berlin, Heidelberg **2007**, p. 305.

[5] Y. Wei, S. Matzen, T. Maroutian, G. Agnus, M. Salverda, P. Nukala, Q. Chen, J. Ye, P. Lecoeur, B. Noheda, *Phys. Rev. Appl.* **2019**, *12*, 031001.
[6] V. Mikheev, A. Chouprik, Y. Lebedinskii, S. Zarubin, Y. Matveyev, E. Kondratyuk, M. G. Kozodaev, A. M. Markeev, A. Zenkevich, D. Negrov, *ACS Appl. Mater. Interfaces* **2019**, *11*, 32108.
[7] Y. Wei, P. Nukala, M. Salverda, S. Matzen, H. J. Zhao, J. Momand, A. S. Everhardt, G. Agnus, G. R. Blake, P. Lecoeur, B. J. Kooi, J. Íñiguez, B. Dkhil, B. Noheda, *Nat. Mater.* **2018**, *17*, 1095.
[8] P. Nukala, M. Ahmadi, Y. Wei, S. De Graaf, E. Stylianidis, T. Chakrabortty, S. Matzen, H. W. Zandbergen, A. Björling, D. Mannix, D. Carbone, B. Kooi, B. Noheda, *Science (80-.)*. **2021**, *372*, 630.
[9] H.-J. Lee, M. Lee, K. Lee, H. Yang, Y. Kim, S. C. Chae, U. Waghmare, J. H. Lee, *Science (80-.)*. **2020**, *369*, 1343.
[10] T. Shimizu, K. Katayama, T. Kiguchi, A. Akama, T. J. Konno, O. Sakata, H. Funakubo, *Sci. Rep.* **2016**, *6*, 32931.
[11] Y. Wei, S. Matzen, C. P. Quinteros, T. Maroutian, G. Agnus, P. Lecoeur, B. Noheda, *npj Quantum Mater.* **2019**, *4*, 62.
[12] T. Schenk, N. Godard, A. Mahjoub, S. Girod, A. Matavz, V. Bobnar, E. Defay, S. Glinsek, *Phys. Status Solidi Rapid Res. Lett.* **2020**, *14*, 1900626.
[13] J. Liu, S. Liu, J. Yang, L. Liu, *Phys. Rev. Lett.* **2020**, *125*, 197601.
[14] J. Liu, S. Liu, L. H. Liu, B. Hanrahan, S. T. Pantelides, *Phys. Rev. Appl.* **2019**, *12*, 034032.
[15] S. Dutta, P. Buragohain, S. Glinsek, C. Richter, H. Aramberri, H. Lu, U. Schroeder, E. Defay, A. Gruverman, J. Íñiguez, *Nat. Commun.* **2021**, *12*, 7301.
[16] R. Korobko, A. Patlolla, A. Kossoy, E. Wachtel, H. L. Tuller, A. I. Frenkel, I. Lubomirsky, *Adv. Mater.* **2012**, *24*, 5857.
[17] N. Yavo, D. A. Smith, O. Yeheskel, R. S. Cohen, R. Korobko, E. Wachtel, R. P. Slater, I. Lubomirsky, *Adv. Funct. Mater.* **2016**, *16*, 1138.
[18] S. Santucci, H. Zhang, A. Kabir, C. Marini, S. Sanna, J. K. Han, G. Ulbrich, E. M. Heppke, I. E. Castelli, V. Esposito, *Phys. Chem. Chem. Phys.* **2021**, *23*, 11233.
[19] H. Zhang, N. Pryds, D. S. Park, N. Gauquelin, S. Santucci, D. V. Christensen, D. Jannis, D. Chezganov, D. A. Rata, A. R. Insinga, I. E. Castelli, J. Verbeeck, I. Lubomirsky, P. Muralt, D. Damjanovic, V. Esposito, *Nature* **2022**, *609*, 695.
[20] M. D. Glinchuk, A. N. Morozovska, A. Lukowiak, W. Stręk, M. V. Silibin, D. V. Karpinsky, Y. Kim, S. V. Kalinin, *J. Alloys Compd.* **2020**, *830*, 153628.
[21] C. Lichtensteiger, *J. Appl. Crystallogr.* **2018**, *51*, 1745.
[22] Y. Kadota, H. Hosaka, T. Morita, *Ferroelectrics* **2008**, *368*, 185.
[23] S. Santucci, H. Zhang, S. Sanna, N. Pryds, V. Esposito, *J. Mater. Chem. A* **2020**, *8*, 14023.
[24] D. Carbone, S. Kalbfleisch, U. Johansson, A. Björling, M. Kahnt, S. Sala, T. Stankevic, A. Rodriguez-Fernandez, B. Bring, Z. Matej, P. Bell, D. Erb, V. Hardion, C. Weninger, H. Al-Sallami, J. Lidon-Simon, S. Carlson, A. Jerrebo, B. N. Jensen, A. Bjermo, K. Åhnberg, L. Roslun, *J. Synchrotron. Radiat.* **2022**, *29*, 876.
[25] D. Carbone, A. I. Pateras, G. Bussone, P. G. Evans, T. W. Cornelius, M. Bousquet, A. Boulle, B. Gautier, J. R. Duclere, *Appl. Phys. Lett.* **2014**, *105*, 242901.
[26] G. Kresse, J. Furthmüller, *Phys. Rev. B Condens. Matter Mater. Phys.* **1996**, *54*, 11169.
[27] G. Kresse, D. Joubert, *Phys. Rev. B Condens. Matter Mater. Phys.* **1999**, *59*, 1758.
[28] J. P. Perdew, A. Ruzsinszky, G. I. Csonka, O. A. Vydrov, G. E. Scuseria, L. A. Constantin, X. Zhou, K. Burke, *Phys. Rev. Lett.* **2008**, *100*, 136406.
[29] P. E. Blöchl, *Phys. Rev. B* **1994**, *50*, 17953.
[30] X. Wu, D. Vanderbilt, D. R. Hamann, *Phys. Rev. B Condens. Matter Mater. Phys.* **2005**, *72*, 035105.
[31] R. D. King-Smith, D. Vanderbilt, *Phys. Rev. B* **1993**, *47*, 1651.